Origin of the diagonal double-stripe spin density wave and potential superconductivity in bulk $La_3Ni_2O_7$ at ambient pressure

Yu-Bo Liu,[1,*] Hongyi Sun,[2,3,*] Ming Zhang,[4,*] Qihang Liu,[5,6] Wei-Qiang Chen,[7,8,†] and Fan Yang[1,‡]

[1]*School of Physics, Beijing Institute of Technology, Beijing 100081, China*
[2]*Shenzhen Institute for Quantum Science and Engineering, Southern University of Science and Technology, Shenzhen 518055, China*
[3]*International Quantum Academy, Shenzhen 518048, China*
[4]*Zhejiang Key Laboratory of Quantum State Control and Optical Field Manipulation, Department of Physics, Zhejiang Sci-Tech University, 310018 Hangzhou, China*
[5]*Department of Physics, Southern University of Science and Technology, Shenzhen 518055, China*
[6]*Shenzhen Key Laboratory of Advanced Quantum Functional Materials and Devices, Southern University of Science and Technology, Shenzhen 518055, China*
[7]*State Key Laboratory of Quantum Functional Materials and Department of Physics, Southern University of Science and Technology, Shenzhen 518055, China*
[8]*Quantum Science Center of Guangdong-Hong Kong-Macao Greater Bay Area, Shenzhen 518045, China*

(Received 24 January 2025; revised 24 April 2025; accepted 26 June 2025; published 14 July 2025)

The discovery of high-temperature superconductivity (SC) with $T_c \approx 80$ K in the pressurized $La_3Ni_2O_7$ has aroused great interest. Currently, due to technical difficulties, most experiments on $La_3Ni_2O_7$ can only be performed at ambient pressure. Particularly, various experiments have revealed the presence of a spin density wave (SDW) in the unidirectional diagonal double-stripe pattern with wave vector near $\pm(\pi/2, \pi/2)$ in $La_3Ni_2O_7$ at ambient pressure. In this work, we employ first-principles calculations followed by the random phase approximation (RPA)-based study to clarify the origin of this special SDW pattern and the potential SC in $La_3Ni_2O_7$ at ambient pressure. Starting from our density-functional-theory band structure, we construct an eight-band bilayer tight-binding model using the Ni-$3d_{z^2}$ and $3d_{x^2-y^2}$ orbitals, which is equipped with the standard multiorbital Hubbard interaction. Our RPA calculation reveals an SDW order driven by Fermi surface nesting with wave vector $\boldsymbol{Q} \approx (0, \pm 0.84\pi)$ in the folded Brillouin zone. From the view of the unfolded Brillouin zone, the wave vector turns to $\boldsymbol{Q}_0 \approx \pm(0.58\pi, 0.58\pi)$, which is near the one detected by various experiments. Further more, this SDW exhibits an interlayer antiferromagnetic order with a unidirectional diagonal double-stripe pattern, consistent with recent soft x-ray scattering experiments. This result suggests that the origin of the SDW order in $La_3Ni_2O_7$ at ambient pressure can be well understood in the itinerant picture as driven by Fermi surface nesting. In the aspect of SC, our RPA study yields an approximate $s^{\pm}$-wave spin-singlet pairing with T_c much lower than that under high pressure. Furthermore, the T_c can be strongly enhanced through hole doping, leading to possible high-temperature SC at ambient pressure.

DOI: 10.1103/24f4-349n

I. INTRODUCTION

Recently, the experiments [1] have reported that the bilayer nickelate $La_3Ni_2O_7$ exhibits superconductivity (SC) at 80 K under pressures above 14 GPa, which has been confirmed by subsequent experiments [2–9]. Inspired by SC in $La_3Ni_2O_7$, efforts have been made to search for more nickelate superconductors in the Ruddlesden-Popper (RP) phase [10,11], resulting in the discovery of SC in $La_4Ni_3O_{10}$ under high pressure (HP) [12–15]. These discoveries have rapidly sparked research into the electronic structure [16–41], the pairing mechanisms [42–78], and the correlated states [79–87] of nickelate SC materials. The nickelate superconductors, including the pressurized RP-phase $La_3Ni_2O_7$ and $La_4Ni_3O_{10}$ and previously synthesized infinite-layer nickelates $Nd_{1-x}Sr_xNiO_2$ [88–91], have become a new platform for exploring high-temperature SC after cuprates [92–94] and iron-based [95,96] superconductors.

Currently, most experimental investigations on the RP-phase nickelates are carried out at ambient pressure (AP) because the HP circumstance strongly hinders the experimental detection of the physical properties of the materials. It is inspiring that, very recently, evidences of SC with T_c beyond the McMillan limit (40 K) has been reported in the ultrathin $La_3Ni_2O_7$ film at AP [97,98], which will strongly push the development of this field. Therefore studies on the RP-phase nickelates at AP are becoming more and more important. At AP, experiments on the bulk materials of the RP-phase nickelates have uncovered density-wave (DW) orders which compete with the SC, and such competition is key to unraveling the mechanism of SC. Concretely, evidences of charge DW (CDW) and spin DW (SDW) are reported in $La_3Ni_2O_7$ [99–114] and $La_4Ni_3O_{10}$ [99,115–117], catching lots of theoretical interests [118–129].

*These three authors contributed equally to this work.
†Contact author: chenwq@sustech.edu.cn
‡Contact author: yangfan_blg@bit.edu.cn

Here, we focus on the SDW discovered in bulk $La_3Ni_2O_7$ at AP through the muon spin relaxation [100,101], the nuclear magnetic resonance (NMR) [99,102,105], the neutron scattering [106] and the soft x-ray scattering [103,107] measurements. Particularly, the soft x-ray scattering measurements [103,107] reveal the presence of an interlayer antiferromagnetic (AFM) SDW order with an intriguing unidirectional diagonal double-stripe pattern within each layer, with wave vector near $\pm(\pi/2, \pi/2)$. Note that the NMR [102] measurements suggest that such a stripy SDW order is a pure spin order, without coexisting CDW order. To fit the experimentally detected magnon dispersion of this SDW state with linear spin wave theory, an attempt based on the local moment description of the SDW order has been made, resulting in a Heisenberg spin model with various superexchange interactions, among which the interlayer superexchange interaction is more than an order of magnitude stronger than the intralayer ones [103]. However, such a Heisenberg spin model is problematic because if the interlayer superexchange interaction really overwhelms the intralayer one, the interlayer dimer state would be formed, instead of the SDW ordered state. The unreasonable fitting result of the SDW order based on the local moment description necessitates the itinerant description of the SDW order.

Various theoretical attempts have been made to clarify the origin of the SDW order with the diagonal double-stripe pattern based on the itinerant picture. The random phase approximation (RPA) calculations [126] adopting the tight-binding (TB) parameters for the HP phase yield an SDW wave vector distinct from the experimental one, suggesting that the magnetic structures under HP and AP are distinct, which necessitates the investigation of the SDW order in the AP circumstance. Note that the lattice structure and symmetry of $La_3Ni_2O_7$ at AP are different from those under HP, particularly with doubled unit cell. The unbiased density-functional-theory (DFT) calculations [129,130] obtained ferromagnetic or A-type AFM phase as the ground state, which is not consistent with the experiments. The dynamic-mean-field-theory [86] or DFT [119–121] based calculations have provided the energies corresponding to a few candidate SDW patterns within a 4×4 expanded magnetic unit cell associated with the assumed or calculated wave vector $\pm(\pi/2, \pi/2)$, resulting in the conclusion that the diagonal double-stripe pattern is really the energetically favored one. However, within 4×4 expanded unit cell, the magnetic moment at every site can take independent and arbitrary values. These calculations are somewhat biased as only a few candidate SDW patterns have been investigated among the infinite number of possible ones within the 4×4 magnetic unit cell. Note that an arbitrary 4×4 pattern will usually lead to not only a peak at $\pm(\pi/2, \pi/2)$ but also peaks at the higher harmonic components of this wave vectors, e.g., $(\pi/2, \pi)$ or (π, π), while the experiments on $La_3Ni_2O_7$ at AP have only discovered the one $\pm(\pi/2, \pi/2)$ [103,107]. It is the purpose of the present study to reveal the origin of the special SDW pattern observed in experiments, including the wave vector near $\pm(\pi/2, \pi/2)$ and the unique unidirectional diagonal double-stripe pattern, from unbiased first-principles calculations without assuming any candidate patterns.

In this paper, we carry out an unbiased first-principles study on the properties of the SDW and the potential SC in $La_3Ni_2O_7$ at AP. In Sec. II, we start by constructing a bilayer eight-band TB model, obtained by Wannier fitting of our first-principles DFT+U band structure, using the Ni-$3d_{z^2}$ and $3d_{x^2-y^2}$ orbitals. Then, in Sec. III, after considering the standard multi-orbital Hubbard interaction, we perform a RPA based study on the properties of the SDW order of the system. Our result reveals an SDW order with wave vector $\boldsymbol{Q} \approx (0, \pm 0.84\pi)$ in the folded Brillouin zone (BZ), which turns into $\boldsymbol{Q}_0 \approx \pm(0.58\pi, 0.58\pi)$ in the unfolded BZ, near the $\pm(\pi/2, \pi/2)$ detected by experiments. The real-space distribution of the magnetic moment of the SDW takes the unidirectional diagonal double-stripe pattern, with the moments in the two NiO_2 planes AFM aligned. Such an SDW pattern is well consistent with experiments. In Sec. III, we further study the potential SC at AP via the RPA approach, which shows that the T_c at AP is lower than that under HP, consistent with experiments. Furthermore, our RPA result predicts that the T_c will be enhanced with hole doping at AP. Section V provides the discussion and conclusion.

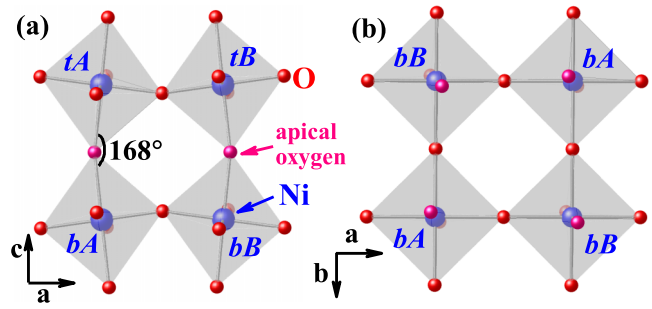

FIG. 1. The schematic of the crystal structure of $La_3Ni_2O_7$ at AP, where red, pink, and blue spheres represent O, apical oxygen, and Ni atoms, respectively, and gray lines represent Ni-O bonds. (a) is the side view of the bilayer crystal and (b) is the top view of the bottom layer crystal. The interlayer Ni-O-Ni bonding angle is 168°, marked in (a).

II. DFT BAND STRUCTURE AND THE MICROSCOPIC MODEL

In $La_3Ni_2O_7$, each conventional unit cell contains four NiO layers[1], including the weakly coupled isostructural upper and lower bilayers separated by a LaO layer. The lattice structure of each bilayer is shown in Fig. 1. In this structure, around each Ni atom, there are six oxygen atoms which form a standard octahedron. The two NiO layers stacking along the c-axis are named as the top (t) and bottom (b) layer, respectively. Each Ni atom in the top layer is connected to a Ni atom in the bottom layer via an oxygen atom in the intermediate LaO layer through the interlayer Ni-O-Ni bond. It is important to note that the interlayer Ni-O-Ni bonding angle at AP is 168°, which is different from 180° under HP. Such a difference leads to different lattice symmetries between the AP and HP phases: under HP, the lattice structure belongs to the $Fmmm$ phase which possesses C_4 rotation symmetry and each unit cell contains one Ni atom in each layer. However, at AP, the lattice structure belongs to the $Amam$ phase, in which the octahedrons associate with the Ni atoms in the a-b plane alternately tilt toward two different directions, dividing the original

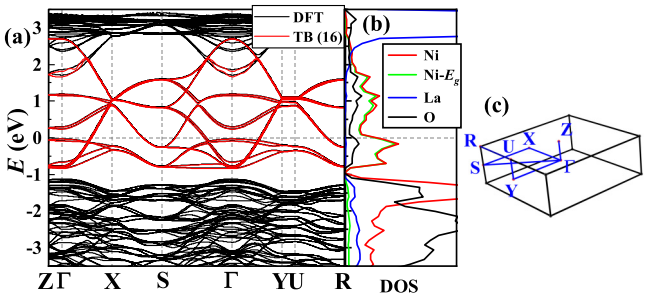

FIG. 2. (a) DFT band structure (black lines) for $La_3Ni_2O_7$ at AP, in comparison with the sixteen-band TB band structure (red lines) obtained through Wannier fitting. Experimentally refined lattice constants are adopted in the DFT calculation. (b) The DOS near the Fermi energy, contributed by Ni (red), the E_g orbitals of Ni (green), La (blue), and O (black) atoms. (c) Schematic of the 3D BZ. Several high-symmetry points are marked in the BZ.

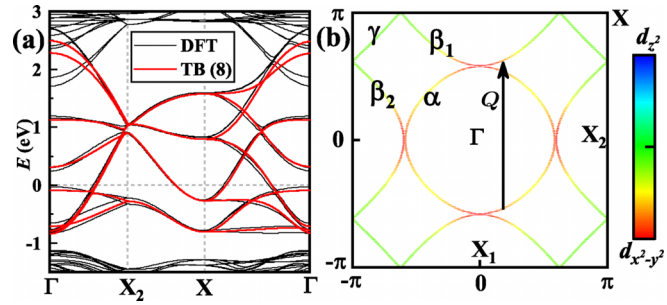

FIG. 3. Band structure and Fermi surfaces (FSs) of $La_3Ni_2O_7$ at AP obtained from the eight-band TB-model Eq. (1). (a) The band structure of the eight-band TB-model (red line) along the high-symmetry lines, compared with the DFT band structure (black line). (b) FSs in the folded BZ, marked by α, β_1, β_2, and γ. The color in (b) indicates the orbital weight of $d_{x^2-y^2}$ and d_{z^2}. The FS-nesting vector is marked by $\boldsymbol{Q}$.

Bravais lattice within each layer into two unequal sublattices labeled as A and B respectively, as shown in Figs. 1(a) and 1(b). Meanwhile, the lattice lacks the C_4 rotation symmetry.

We have performed a DFT based calculation for the band structure of $La_3Ni_2O_7$ at AP, taking the experimentally detected lattice structure and the lattice constant [131]. The DFT calculations are performed based on the projector-augmented wave (PAW) pseudopotentials with the exchange correlation of the Perdew-Burke-Ernzerhof and the GGA + U approach, as implemented in the Vienna *ab initio* simulation package (VASP) [132–135]. Starting from the *Amam* crystal structure with experimentally measured lattice constants at AP [131], we fix the lattice constants and optimize the positions of atoms within the conventional unit cell until the force acting on each atom is less than 10^{-3} eV/Å. The cutoff energy is set to be 600 eV, and the k mesh is $19 \times 19 \times 5$. To account for the correlation effects of $3d$ electrons in Ni atoms, an effective $U = 3.5$ eV is chosen, as reported in previous work [16]. Figure 2(a) shows our DFT band structure along the high-symmetric lines in the BZ exhibited in Fig. 2(c). We note that one can also perform DFT calculations within the primitive unit cell, which yields the unfolded version of our band structure. The density of state (DOS) contributed by different chemical elements is shown in Fig. 2(b), which shows that the low-energy DOS near the Fermi level is dominantly contributed by the Ni-$3d$-E_g orbitals. Therefore we project the Bloch electronic states obtained from DFT calculations onto the Ni-$3d_{z^2}/3d_{x^2-y^2}$ orbitals and construct a sixteen-band TB model Hamiltonian in the Wannier representation by using the WANNIER90 code [136]. as shown in Fig. 2(a), the sixteen-band TB band structure thus obtained is well consistent with the DFT one near the Fermi level. At energy far from the Fermi level, the TB bands exhibit deviations from the DFT bands, but such discrepancies do not affect the low-energy properties of the system.

In $La_3Ni_2O_7$ at AP, each conventional unit cell contains four layers, with each layer containing two Ni atoms and each Ni atom containing two $3d$-E_g orbitals, adding up to sixteen effective orbitals. It is important to note that the coupling between the upper bilayer and lower bilayer is very weak because the two bilayers are separated by a LaO layer, as also verified by the weak corresponding band split in the DFT band structure. Taking advantage of this character, we reasonably neglect the coupling between the upper bilayer and the lower one, and approximately take each bilayer as the unit cell to construct a 2D bilayer model. In this model, each unit cell only contains four Ni atoms, labeled as tA, tB, bA, and bB in Fig. 1(a). The Hamiltonian of this eight-band TB model reads

$$H_{\mathrm{TB}} = \sum_{ij,\mu\nu,\sigma} t_{ij,\mu\nu} c^{\dagger}_{i\mu\sigma} c_{j\nu\sigma} + \mathrm{H.c.} + \sum_{i\mu\sigma} \varepsilon_{\mu} c^{\dagger}_{i\mu\sigma} c_{i\mu\sigma}. \quad (1)$$

Here i/j denotes the combined in-plane site, sublattice (A or B) and layer (t or b) index, μ/ν labels orbital ($3d_{z^2}$ or $3d_{x^2-y^2}$) and σ labels spin. ε_{μ} is the on-site energy of orbital μ. The hopping integrals $t_{ij,\mu\nu}$ of this model are extracted from the corresponding ones in the original sixteen-band model, which are provided in Table II and Fig. 7 in Appendix B Similarly with $La_3Ni_2O_7$ under HP, the interlayer hoppings between the d_{z^2} orbitals are the dominant ones.

Figure 3(a) shows the band structure of the above eight-band TB model Eq. (1), in comparison with the DFT band structure. Obviously, despite minor discrepancies in details, the former has captured the essential characteristics of the latter near the Fermi energy, particularly regarding the FS nesting, thereby ensuring the reliability of subsequent results. The FSs of the eight-band TB model are shown in Fig. 3(b), where the color indicates the orbital weight. There are four pockets, including an electron pocket α centered around the Γ point, another small electron pocket γ centered around the X point, and two hole pockets β_1 and β_2 centered around the X_1 and X_2 points, respectively. Both orbital components are significantly involved on the FSs.

The band structure shown in Fig. 3 illustrates three prominent features. (1) In comparison with the band structure under HP shown in Figs. 6(c) and 6(d) in Appendix A in which the bonding d_{z^2} band crosses the Fermi energy to form a hole pocket γ', here at AP the bonding d_{z^2} band shifts below the Fermi energy and the corresponding hole pocket vanishes. This feature of our bands is consistent with other existing bands for AP phase [1,16,83,86] and HP phase [1,20,21,45,46,62,76,77,123,126] $La_3Ni_2O_7$. (2) The electron pocket α is well nested with the hole pocket β_1.

Such FS nesting suggests the potential for DW order at low temperatures, with the nesting vector $\boldsymbol{Q}$ as the wave vector. Note that as the unit cell at AP is doubled from that under HP, the BZ here is the inscribed square of the BZ under HP. (3) At the Γ point, the bonding d_{z^2} band lies very close to the Fermi surface (particularly for the DFT bands). However, since there is no suitable FS that nests with the bonding d_{z^2} band, this band does not contribute to prominent FS nesting.

It is necessary to introduce the electron-electron interaction to investigate the correlated electronic states. We adopt the multiorbital Hubbard interaction,

$$H_{\text{int}} = U \sum_{i\mu} n_{i\mu\uparrow} n_{i\mu\downarrow} + (U - 2J_H) \sum_{i,\sigma,\sigma'} n_{i1\sigma} n_{i2\sigma'} + J_H \sum_{i\sigma\sigma'} [c^\dagger_{i1\sigma} c^\dagger_{i2\sigma'} c_{i1\sigma'} c_{i2\sigma} + (c^\dagger_{i1\uparrow} c^\dagger_{i1\downarrow} c_{i2\downarrow} c_{i2\uparrow} + \text{H.c.})], \tag{2}$$

where the first, second and third terms denote the intraorbital Hubbard repulsion, the interorbital one and the Hund's rule coupling (plus the pair hopping), respectively. We fix $J_H = U/6$ for the subsequent calculations.

The total Hamiltonian adopted in our study is

$$H = H_{\text{TB}} + H_{\text{int}}. \tag{3}$$

To solve this Hamiltonian, we adopt the RPA approach [137–143]. In the RPA approach, by defining the spin susceptibility matrix $\chi^{(s)pq}_{st}(\boldsymbol{k}, i\omega = 0)$, the critical interaction strength $U_c \approx 1.2$ eV for SDW can be provided. For $U < U_c$, the finite spin susceptibility implies short-range spin fluctuations, which can mediate attractive interaction channels for SC. For $U > U_c$, the spin susceptibility diverges, suggesting the onset of SDW order. See Appendix C for details of the RPA approach.

III. PROPERTIES OF THE SDW

We study the properties of the SDW order in $La_3Ni_2O_7$ at AP via the RPA approach, including the wave vector and the distribution pattern of the SDW moment within a unit cell. To obtain the wave vector of the SDW order, we calculate the largest eigenvalue $\chi^{(s)}(\boldsymbol{k})$ of the spin susceptibility matrix $\chi^{(s)pq}_{st}(\boldsymbol{k}, i\omega_n = 0)$. See Appendix C for more details of the spin susceptibility matrix $\chi^{(s)pq}_{st}(\boldsymbol{k}, i\omega_n)$. The $\chi^{(s)}(\boldsymbol{k})$ for $U = 1$ eV is shown in Fig. 4(a). Obviously, the largest $\chi^{(s)}$ is located near the momenta $\boldsymbol{Q} = (0, \pm 0.84\pi)$, which are precisely the nesting vectors between the α and β_1 Fermi pockets, as marked in Fig. 3(b). The second largest spin susceptibility is located at the momenta $\boldsymbol{Q}' = (\pm 0.84\pi, 0)$, corresponding to the nesting vector between the α and β_2 pockets. Note that the wave vectors $\boldsymbol{Q}$ and $\boldsymbol{Q}'$ are not equivalent due to breaking of the C_4 symmetry in $La_3Ni_2O_7$ at AP. Our result yields that the spin susceptibilities $\chi^{(s)}(\boldsymbol{k} = \pm\boldsymbol{Q})$ are always the largest for any value of U and J_H, suggesting that the wave vector of the SDW order in $La_3Ni_2O_7$ at AP should be $\pm\boldsymbol{Q}$. Note that the SDW with wave vector $\boldsymbol{Q}$ and $\boldsymbol{Q}'$ are experimentally indistinguishable, and both correspond to the unidirectional diagonal double-stripe states observed in experiments. Therefore, in the following analysis, we focus primarily on the SDW with vector $\boldsymbol{Q}$, as it effectively represents the one with vector $\boldsymbol{Q}'$ as well.

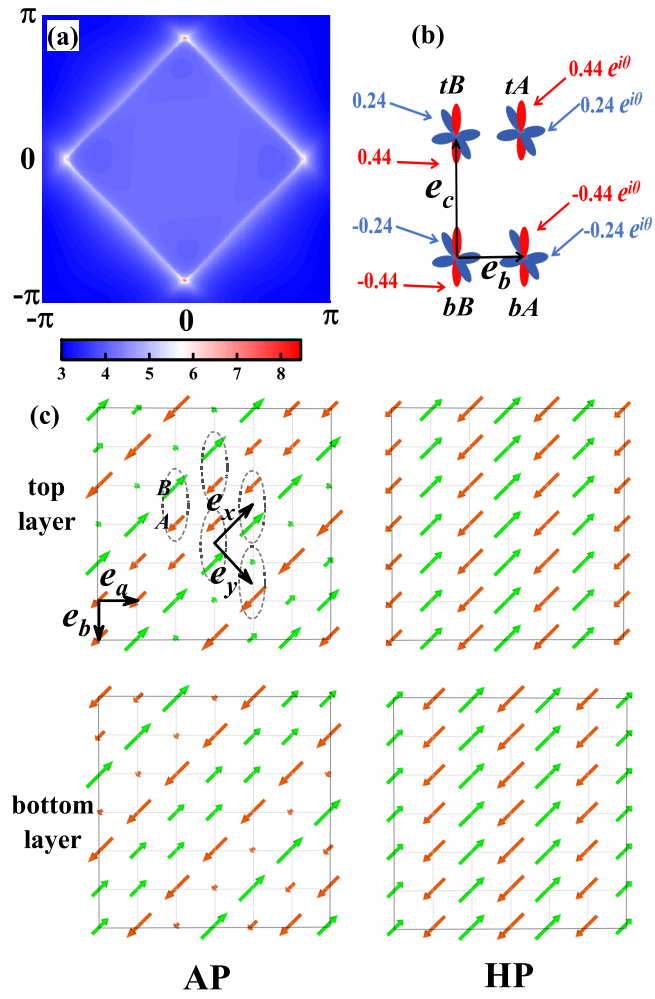

FIG. 4. The wave vector and the pattern of SDW for $La_3Ni_2O_7$ at AP. (a) The distribution of the spin susceptibility $\chi^s(\boldsymbol{k})$ in the folded BZ for $U \approx 1$ eV. The maximal value of $\chi^s(\boldsymbol{k})$ just locates at $\boldsymbol{Q} \approx (0, \pm 0.84\pi)$. (b) The pattern of SDW within an unit cell, in which red (blue) orbital represents Ni-$3d_{z^2}$ ($3d_{x^2-y^2}$) orbital. The eight values in (b) are normalized. The difference between the SDW phases for the sublattice A and B within a unit cell is $\theta \approx 0.58\pi$. (c) Schematic SDW pattern on the whole lattice at AP (left) and under HP (right). In the left panel, each dashed oval represents a unit cell within a layer. The length and orientation/color of the arrows represent the magnitude and sign of the magnetic moment $m_{i\alpha}$, respectively.

The distribution pattern of the magnetic moment within a unit cell is determined by the eigenvector ξ corresponding to the largest eigenvalue of the spin susceptibility matrix $\chi^{(s)}(\boldsymbol{Q}, i\omega_n = 0)$ with $U \to U_c$, see Appendix C for more details. Our numerical results yield that the SDW order here is dominated by the on-site intraorbital magnetism. While the absolute magnitude of the magnetic moment strongly depends on the interaction U, Fig. 4(b) illustrates the distribution pattern of relative magnetic moments within the unit cell. Three features are obvious in this pattern. (1) For each orbital site, the magnetic moment in the top layer is different from that in the bottom layer only by a minus sign, suggesting an interlayer AFM. (2) For each site in each layer, the ratio between

the magnetic moment in the $3d_{x^2-y^2}$ orbital and that in the $3d_{z^2}$ orbital is fixed at about 0.24 : 0.44, suggesting that both orbitals are significantly involved in the SDW order. (3) For each orbital and layer, while the SDW amplitudes of the A and B sites within any unit cell are the same, the difference between their SDW phases is $\theta_A - \theta_B = \theta \approx 0.58\pi$. It is interesting that this value is just very near half of the y component of the wave vector $(0, 2\pi) + \boldsymbol{Q}$.

In the following, we plot the distribution pattern of the SDW moment all over the lattice. Since the ratio between the magnetic moments of the two orbitals is fixed on any site, we can focus on the distribution pattern for any orbital, e.g., $3d_{z^2}$, as a representative in the following. In the SDW ordered state with wave vector $\boldsymbol{Q}$, the average magnetic moment $m_{i\alpha}$ in the ith unit cell in the sublattice α ($\alpha = A/B$) in, say the top layer, is given as,

$$\begin{aligned} m_{i\alpha} &= m_0 \mathrm{Re}\left[e^{i(\boldsymbol{Q}\cdot\boldsymbol{R}_i+\theta_\alpha)}\right] \\ &= m_0 \cos\left(\boldsymbol{Q}\cdot\boldsymbol{R}_i + \theta_\alpha\right), \end{aligned} \tag{4}$$

and that in the bottom layer differs from Eq. (4) by a minus sign. Note that in obtaining Eq. (4), we have used the fact that the SDW amplitudes in both sublattices are equal. Here for convenience, we define

$$\boldsymbol{Q}\cdot\boldsymbol{R}_i + \theta_\alpha \equiv \theta_{i\alpha} \tag{5}$$

as the phase of the SDW at the site in the ith unit cell on the sublattice α. Note that $\theta_{i\alpha}$ does not mean the orientation of the spin vector at site i. The difference between the phases of the A and B sites within a unit cell is $\theta_A - \theta_B = \theta \approx 0.58\pi$. Meanwhile, the wave vector of the SDW order is $\boldsymbol{Q}$ in the folded BZ, which is equally viewed as $(0, 2\pi) + \boldsymbol{Q} = (Q_x, Q_y) \approx (0, 1.16\pi)$. Note that we have $\theta \approx Q_y/2$. The distribution pattern obtained from Eq. (4) is schematically illustrated in the left panel of Fig. 4(c), which clearly exhibits a unidirectional diagonal double-stripe pattern. Here, each unit cell represented by a dashed oval contains the A and B sites, and the $\boldsymbol{e}_x$ and $\boldsymbol{e}_y$ are the unit vectors for this unit cell, while the $\boldsymbol{e}_a$ and $\boldsymbol{e}_b$ are the unit vectors for the original undoubled unit cell. In Fig. 4(c), the length and orientation/color of the arrows represent the magnitude and sign of $m_{i\alpha}$, respectively.

In the left panel of Fig. 4(c), along the $\boldsymbol{e}_x$ direction, $\theta_{i\alpha}$ remains constant because $Q_x = 0$. Consequently, the magnetic moment remains constant along this direction, leading to a diagonal stripe that extends along the $\boldsymbol{e}_x$ direction. Along the $\boldsymbol{e}_y$ direction, $\theta_{i\alpha}$ changes by $Q_y = 1.16\pi$ with each translation by $\boldsymbol{e}_y$. Consequently, the magnetic moment nearly changes by a minus sign with each translation by $\boldsymbol{e}_y$, considering that Q_y is near π. Note that each translation by $\boldsymbol{e}_y$ leads to passing across two stripes. Therefore this distribution pattern just provides the unidirectional diagonal double-stripe pattern shown in the left panel in Fig. 4(c).

Then, let us investigate how the SDW phase $\theta_{i\alpha}$ changes with each translation by $\boldsymbol{e}_a$ or $\boldsymbol{e}_b$, so that to figure out its wave vector in the original unfolded BZ. With a translation by $\boldsymbol{e}_a$, if the translation is from sublattice A to B, $\theta_{i\alpha}$ changes by

$$[(\boldsymbol{R}_i + \boldsymbol{e}_y)\cdot\boldsymbol{Q} + \theta_B] - (\boldsymbol{R}_i\cdot\boldsymbol{Q} + \theta_A) = Q_y - \theta, \tag{6}$$

and if it is from B to A, $\theta_{i\alpha}$ changes by

$$[(\boldsymbol{R}_i + \boldsymbol{e}_x)\cdot\boldsymbol{Q} + \theta_A] - (\boldsymbol{R}_i\cdot\boldsymbol{Q} + \theta_B) = Q_x + \theta = \theta. \tag{7}$$

With the translation by $\boldsymbol{e}_b$, if the translation is from sublattice A to B, the SDW phase $\theta_{i\alpha}$ changes by

$$\begin{aligned} &[(\boldsymbol{R}_i + \boldsymbol{e}_y - \boldsymbol{e}_x)\cdot\boldsymbol{Q} + \theta_B] - (\boldsymbol{R}_i\cdot\boldsymbol{Q} + \theta_A) \\ &= Q_y - Q_x - \theta = Q_y - \theta, \end{aligned} \tag{8}$$

and if it is from B to A, $\theta_{i\alpha}$ changes by

$$(\boldsymbol{R}_i\cdot\boldsymbol{Q} + \theta_A) - (\boldsymbol{R}_i\cdot\boldsymbol{Q} + \theta_B) = \theta. \tag{9}$$

Interestingly, as $\theta \approx Q_y/2$, we have $Q_y - \theta \approx \theta \approx 0.58\pi$. Therefore, with each translation by $\boldsymbol{e}_a$ or $\boldsymbol{e}_b$, the SDW phase changes approximately 0.58π, suggesting that the SDW wave vector in the unfolded BZ should be approximately $\boldsymbol{Q}_0 = \pm(0.58\pi, 0.58\pi)$.

The obtained SDW wave vector $\boldsymbol{Q}_0 = \pm(0.58\pi, 0.58\pi)$ in the unfolded BZ is close to the value $\pm(0.5\pi, 0.5\pi)$ revealed by various experiments [102,103,107], and the interlayer AFM SDW order with unidirectional diagonal stripe pattern shown in the left panel of Fig. 4(c) is consistent with the experiment of soft x-ray scattering [103,107]. Such consistency between our RPA results and the experimental observations suggests that the origin of the SDW order in $La_3Ni_2O_7$ at AP can be well understood in the itinerant picture as being induced by FS nesting. For comparison, the distribution of the magnetic moment under HP is schematically illustrated in the right panel of Fig. 4(c), which exhibits a stripe pattern extending along the $\boldsymbol{e}_b$ direction with the wave vector $\boldsymbol{Q}_1 \approx (0.9\pi, 0)$ [43] in the unfolded BZ. Such an SDW order originates from the FS nesting between the γ' and β' pockets in the unfolded BZ, as shown in Fig. 6(d) in Appendix A.

IV. POTENTIAL SC

Currently, no definite evidence of SC has been reported in bulk $La_3Ni_2O_7$ at AP. Here, we explore the potential SC in this system for the following two reasons. On the one hand, it cannot be excluded that SC with a lower T_c can exist in the ideal pure material, which is nevertheless suppressed by ingredients such as oxygen deficiency and impurities in the samples currently synthesized. On the other hand, the SDW detected at AP can also be short-range order. In the framework of RPA [137–143], SC emerges when $U < U_c$, which is mediated by short-range spin fluctuations. In RPA, the pairing nature is characterized by the pairing eigenvalue λ, which is related to the T_c via $T_c \propto e^{-1/\lambda}$, and the pairing symmetry is determined by the eigenvector of the linearized gap equation corresponding to its largest eigenvalue λ. See Appendix C for more details on RPA treatment of SC.

The U-dependent pairing eigenvalue λ for $La_3Ni_2O_7$ at AP (solid lines) is shown in Fig. 5(a), in comparison with that under HP (dashed lines). For $La_3Ni_2O_7$ under HP, whose band structure is given in Appendix A, the D_4 point group symmetry is present. In such a situation, the pairing symmetries include the s-wave, the d-wave, and the doubly degenerate (p_x, p_y) wave, and Fig. 5(a) shows that the s-wave is the leading pairing symmetry. Our result regrading the pairing mechanisms in $La_3Ni_2O_7$ under HP aligns with most theoretical studies [23,24,42,43,45,46,50,51,53–55,57,59,61,64,74,75,78]. Meanwhile, several theoretical studies [52,56] suggest d-wave SC as the leading state, while

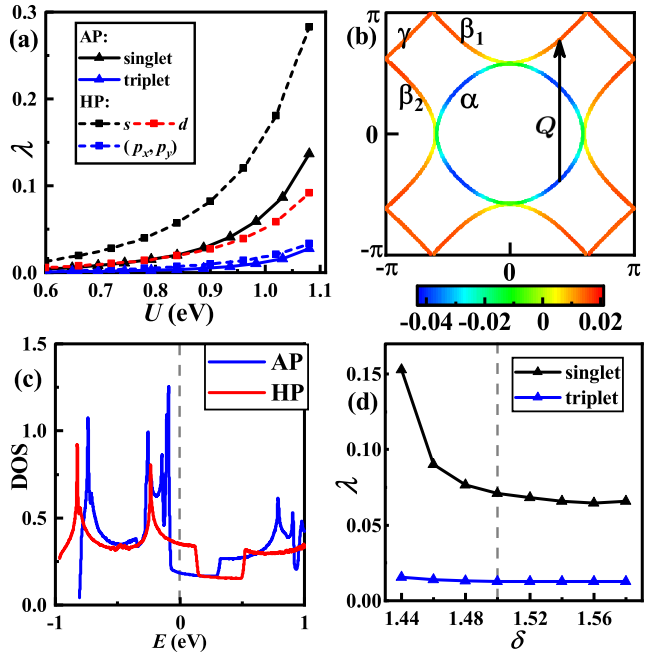

FIG. 5. (a) The largest pairing eigenvalue λ for $La_3Ni_2O_7$ at AP (solid lines) and HP (dashed lines) as a function of U for different pairing symmetries. (b) Distribution of the leading pairing gap function on the FS for $U = 1$ eV. The FS-nesting vector is marked by $\boldsymbol{Q}$. (c) The DOS of $La_3Ni_2O_7$ under HP (red) and at AP (blue). (d) The largest pairing eigenvalue λ at $U = 1$ eV for the spin-singlet (black) and spin-triplet (blue) pairings as functions of the electron number δ per site. The dashed line in (c) and (d) marks the undoped case. The results presented in (b) and (d) are obtained at AP.

Refs. [44,47–49,67,77] proposes competition between s-wave and d-wave SC. At AP, since the D_4 point group symmetry is absent, the pairing symmetries can only be distinguished as spin singlet and spin triplet. Figure 5(a) shows that the spin-singlet pairing is the leading pairing state. The distribution of the pairing gap function on the FS is shown in Fig. 5(b). This pairing gap function is very close to an $s^{\pm}$-wave one, despite the lack of exact C_4 symmetry. The pockets α and β_1, connected by the nesting vector $\boldsymbol{Q}$, are distributed with the strongest pairing amplitude, with their pairing gap signs opposite.

Comparing the two sets of results for AP and HP in Fig. 5(a), it can be observed that for any value of U, the leading λ at AP is considerably smaller than that under HP. This result is consistent with experimental findings that high-T_c SC has only been detected in $La_3Ni_2O_7$ under HP, and implies that SC with lower T_c may exist at AP. In the following, we attempt to provide the physical explanation for the smaller λ at AP, by comparing the band structures under HP and at AP. Under HP, The bonding d_{z^2}-band crosses the Fermi energy and forms a hole pocket γ', as shown in Figs. 6(c) and 6(d) in Appendix A. In contrast, at AP, the bonding d_{z^2}-band shifts below the Fermi energy, and consequently the corresponding hole pocket vanishes, as shown in Fig. 3. This significant difference affects SC in two aspects. Firstly, as shown in Fig. 5(c), the DOS near the Fermi energy at AP is lower than that under HP. Secondly, the γ' pocket under HP provides another FS-nesting vector $\boldsymbol{Q}_1$ between the β' and γ' pockets, as shown in Fig. 6(d) in Appendix A, which contributes significantly to SC under HP[42,43]. In contrast, the absence of this pocket at AP, as shown in Fig. 3, considerably suppresses SC. Recently, ARPES measurements [144] reveal the absence of the γ' pocket in thin $La_2PrNi_2O_7$ films, which may partially explain why the superconducting Tc of the thin film is lower than that of the $La_3Ni_2O_7$ under HP.

The impact of FS on the SC motivates us to investigate the effects of doping on SC. Our results are shown in Fig. 5(d), where the x axis represents the number δ of electrons per site, with $\delta = 1.5$ corresponding to the undoped state. The pairing eigenvalue λ of the triplet pairing is always much smaller than that of the singlet pairing for all δ, indicating that only singlet pairing is possible in this material. For the singlet pairing, the λ remains almost unchanged under electron doping. Under hole doping, λ first slowly increases with the enhancement of the doping until δ reaches 1.45 where λ promptly increases. The reason for the prompt enhancement of λ for $\delta < 1.45$ lies in the abrupt enhancement of the DOS shown in Fig. 5(c), which originates from that the bonding d_{z^2}- band top touches the Fermi level at this doping. This result suggests that high-T_c SC can be achieved in $La_3Ni_2O_7$ at AP through proper hole doping.

V. DISCUSSION AND CONCLUSION

In our study, we construct the band structures through DFT+U calculations, and further employ the RPA method to investigate the nature of the SDW and SC states in $La_3Ni_2O_7$. In the DFT+U calculations, we adopt a larger $U = 3.5$ eV to correct for on-site Coulomb interactions in strongly correlated systems. In the RPA calculations, under the constraint $U < U_c$, a smaller $U \approx 1$ eV is used to account for screening effects and to avoid overestimating correlation effects. Similar to iron-based superconductors, $La_3Ni_2O_7$ is a multiband system with a large bandwidth (∼4 eV). Thus, despite the relatively strong interactions, a weak-coupling approach like RPA is valid for capturing part of the physics of the system.

The SDW wave vector $\boldsymbol{Q}_0 \approx \pm(0.58\pi, 0.58\pi)$ obtained here slightly deviates from the $\pm(0.5\pi, 0.5\pi)$ detected experimentally. This might be caused by strong electron correlation neglected in our weak-coupling RPA approach. In the weak-coupling limit, the SDW wave vector would be exactly given as the FS-nesting vector, which is usually incommensurate. However, in the presence of strong electron interaction, some certain local SDW pattern would be energetically favored, which usually leads to formation of commensurate DW order. For realistic material, the SDW order might probably choose a commensurate wave vector near the FS-nesting vector, and consequently leads to the deviation between the SDW wave vector obtained here and that detected by experiments.

In summary, we have systematically studied the SDW and potential SC for bulk $La_3Ni_2O_7$ at AP. By fitting the DFT band structure, the TB model at AP is obtained. Then we study the magnetic states through the RPA approach. Our results suggest the interlayer AFM SDW, hosting a special unidirectional diagonal double-stripe pattern with an in-plane wave vector $\boldsymbol{Q}_0 \approx \pm(0.58\pi, 0.58\pi)$, which is qualitatively consistent with experiments. Such SDW state originates from the FS nesting.

We have further studied the potential SC for $La_3Ni_2O_7$ at AP, obtaining an approximate $s^{\pm}$-wave SC with T_c lower than that under HP. Inspiringly, we find that hole doping can enhance the T_c.

ACKNOWLEDGMENTS

We are grateful to the discussions with Chen Lu. This work is supported by the National Natural Science Foundation of China (NSFC) under Grants No. 12234016, No. 12074031, No. 12141402, and No. 12334002, Guangdong province Grant (No.2020KCXTD001), Shenzhen Science and Technology Program under Grant No. RCJC20221008092722009. W.-Q. Chen is supported by the National Key R&D Program of China (Grants No. 2024YFA1408101), Guangdong Provincial Quantum Science Strategic Initiative Grand No. SZZX2401001, the SUSTech-NUS Joint Research Program, the Science, Technology and Innovation Commission of Shenzhen Municipality (No. ZDSYS20190902092905285), and Center for Computational Science and Engineering of Southern University of Science and Technology. Ming Zhang is supported by Zhejiang Provincial Natural Science Foundation of China under Grant No. ZCLQN25A0402.

DATA AVAILABILITY

The data supporting this study's findings are available within the article.

APPENDIX A: DFT BAND AND THE TIGHT-BINDING MODEL FOR $La_3Ni_2O_7$ UNDER HIGH PRESSURE

This section presents the results of the density-functional-theory (DFT) and tight-binding (TB) models for $La_3Ni_2O_7$ under high pressure (HP). The DFT calculations for the HP phase are similar to those for the ambient pressure (AP) phase as described in the main text, except that we start from the high-pressured (29.5 Gpa) crystal structure with the measured lattice constants [1] and set the Kmesh to be $13 \times 13 \times 12$ to sample the Brillouin zone of the primitive unit cell. The obtained DFT band structure is shown in Fig. 6(a).

Focusing on the $3d$-E_g orbitals of Ni atoms, similarly to the case of AP, we construct a bilayer two-orbital TB model. The TB Hamiltonian can also be expressed as Eq. (1) in the main text, with the hopping integrals $t_{ij,\mu\nu}$ are provided in Table I and Fig. 6(b). For $La_3Ni_2O_7$ under HP, since the apical Ni-O-Ni bond approaches 180°, each Ni atom within the layer is in an identical environment. The unit cell contains one Ni atom per layer, ultimately resulting in a four-band TB model.

TABLE I. The value of four-band TB hopping parameters for $La_3Ni_2O_7$ under HP. In the superscript and subscript, $x(z)$ represents the $d_{x^2-y^2}(d_{z^2})$ orbit, $\perp$ represents interlayer hopping, and 1,2 represents the NN and NNN hopping, respectively. ϵ is on-site energy. The unit of all parameters is eV.

t_1^x	t_2^x	$t_\perp^x$	t_3^{xz}	ϵ_x
−0.490	0.073	0.008	0.244	0.512
t_1^z	t_2^z	$t_\perp^z$	t_4^{xz}	ϵ_z
−0.119	−0.017	−0.670	−0.031	0

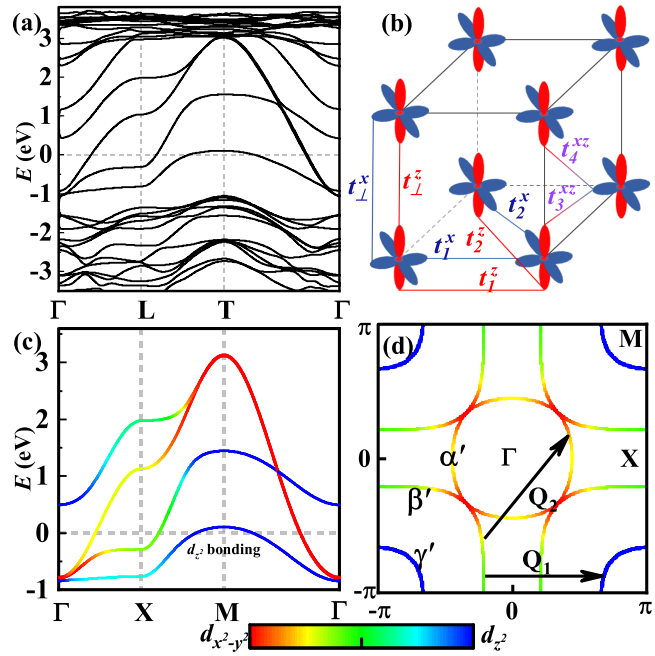

FIG. 6. The DFT band structure and four-band TB model for $La_3Ni_2O_7$ under HP. (a) The DFT band structure, with experimental refined lattice constants adopted. (b) Schematic of the hopping integrals for the bilayer four-band TB model. The red (bule) orbitals represent Ni-d_{z^2}($d_{x^2-y^2}$) orbitals. (c) The TB band structure along the high-symmetry lines. (d) the FS in the BZ, marked by α', β', and γ'. The color in (c) and (d) indicates the orbital weight of d_{z^2} and $d_{x^2-y^2}$.

In Fig. 6(b), all the hopping integrals $t_{ij,\mu\nu}$ are illustrated. Here, the red, blue, and purple lines represent the hopping on the d_{z^2} orbital, the $d_{x^2-y^2}$ orbital, and between two orbitals, respectively. The corner mark x/z indicates $d_{x^2-y^2}/d_{z^2}$ orbitals, $1/2$ indicates nearest-neighbor (NN) /next-nearest-neighbor (NNN) intralayer hopping, and $\perp$ means interlayer hopping. The values of all the hopping integrals are listed in Table I.

Figure 6(c) shows the bands obtained from the TB model, which successfully capture the essential characteristics of the DFT bands. We notice that the d_{z^2}-orbital bonding band crosses the Fermi energy. The corresponding Fermi surfaces (FSs) are shown in Fig. 6(d). There are three pockets, including an electron pocket α', an hole pocket β', and a hole pocket γ', in which the pocket γ' is almost entirely contributed by the d_{z^2} orbital. Interestingly, there are several FS nestings. The FS-nesting between α' and β' pockets is marked as $\boldsymbol{Q}_2$, which qualitatively corresponds to the nesting vector $\boldsymbol{Q}$ for AP as shown in Fig. 3(b) in the main text. The FS nesting between α' and γ' pockets, marked as $\boldsymbol{Q}_1$, is considered to contribute significantly to SC [42,43].

APPENDIX B: TB HOPPING INTEGRALS FOR $La_3Ni_2O_7$ AT AMBIENT PRESSURE

This scetion provides the TB hopping parameters for $La_3Ni_2O_7$ at AP. The hopping integrals $t_{ij,\mu\nu}$ up to NNN are illustrated in Fig. 7(a), with the corner marks having the same

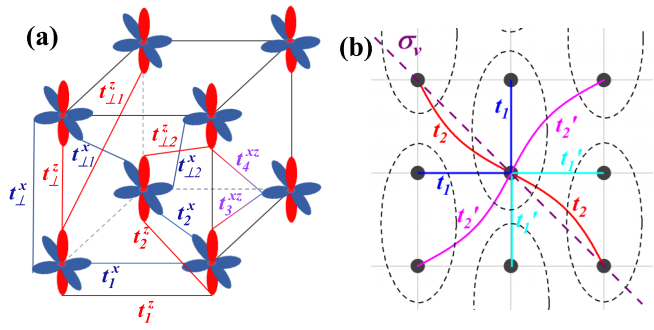

FIG. 7. Schematic of the hopping integrals for $La_3Ni_2O_7$ at AP. (a) Schematic of the main hopping integrals for the eight-band TB model, in which the third-nearest-neighbor hopping integrals ($t_3^{x/z}$ in Table II) are not shown. For $La_3Ni_2O_7$ at AP, the hoping integrals along different directions may be different, but for brevity, they are represented by the same symbol in (a). (b) All the NN and NNN hoping integrals in (a) along different directions. Based on the lattice symmetry, the NN hopping integrals t_1(or NNN hopping integrals t_2) can be divided into two sets, labeled as t_1 and t_1' (or t_2 and t_2'). The gray dots and dashed ovals represent Ni atoms and the unit cell in the a-b plane, respectively. σ_v represents the mirror inversion symmetry of the lattice.

meaning as in Tab. I. For $La_3Ni_2O_7$ at AP, the planform of lattice is shown in Fig. 7(b), the lattice lacks D_4 point group symmetry but has the mirror inversion symmetry σ_v. Based on the lattice symmetry, the four NN hopping integrals t_1(or NNN hopping integrals t_2) can be divided into two sets, labeled as t and t', as shown in Fig. 7(b). The dashed ovals represent a unit cell. The values of all the hopping integrals are listed in Table II.

APPENDIX C: RPA

In the standard multiorbital RPA approach, the bare susceptibility is defined as

$$\chi_{st}^{(0)pq}(\boldsymbol{k},\tau) \equiv \frac{1}{N}\sum_{\boldsymbol{k}_1\boldsymbol{k}_2}\langle T_\tau c_p^\dagger(\boldsymbol{k}_1,\tau)c_q(\boldsymbol{k}_1+\boldsymbol{k},\tau) \times c_s^\dagger(\boldsymbol{k}_2+\boldsymbol{k},0)c_t(\boldsymbol{k}_2,0)\rangle_0, \tag{C1}$$

where $\langle\cdots\rangle_0$ represents the expectation value in the free-electron state, and $p/q/s/t = 1,\ldots,8$ are the effective orbital indices, which label combined layer, sublattice and physical orbital indices. Transforming the above defining formula to the momentum-frequency space, we obtain the explicit formula of bare susceptibility as

$$\chi_{st}^{(0)pq}(\boldsymbol{k},i\omega_n) = \frac{1}{N}\sum_{\boldsymbol{k}_1\alpha\beta}\xi_{p\alpha}^*(\boldsymbol{k}_1)\xi_{q\beta}(\boldsymbol{k}_1+\boldsymbol{k})\xi_{s\beta}^*(\boldsymbol{k}_1+\boldsymbol{k}), \times \xi_{t\alpha}(\boldsymbol{k}_1)\frac{f\left(\varepsilon_{\boldsymbol{k}_1+\boldsymbol{k}}^\beta-\mu_c\right)-f\left(\varepsilon_{\boldsymbol{k}_1}^\alpha-\mu_c\right)}{i\omega_n+\varepsilon_{\boldsymbol{k}_1}^\alpha-\varepsilon_{\boldsymbol{k}_1+\boldsymbol{k}}^\beta}, \tag{C2}$$

where α,β represent band indices; ε and ξ are the eigenvalue and eigenstate of the free particle Hamiltonian; μ_c is the chemical potential, and $f(\varepsilon_{\boldsymbol{k}}) = 1/(1+e^{\beta\varepsilon_{\boldsymbol{k}}})$ is the Fermi-Dirac function. Note that the value of χ do not obviously change with T at low temperatures. Therefore we set $K_BT = 10^{-3}$ eV to represent low temperatures.

In the RPA level, the renormalized spin susceptibility reads

$$\chi^{(s)}(\boldsymbol{k},iw_n) = [I-\chi^{(0)}(\boldsymbol{k},iw_n)U^s]^{-1}\chi^{(0)}(\boldsymbol{k},iw_n), \tag{C3}$$

where the matrix U^s can be found in previous RPA works [137–143]. The critical interaction U_c is defined as the value of U under which Eq. (C3) begins to diverge, that is, the largest eigenvalue of the matrix $\chi^{(0)}(\boldsymbol{k},iw_n)U^s$ begins to touch 1 at some certain $\boldsymbol{k}$. When $U > U_c$, the SDW order is formed, while at $U < U_c$ the SC would emerge which is mediated by the short-range spin fluctuation.

The properties of the SDW order for $U > U_c$ can be obtained as follows. Setting $U \to U_c$ from below, let us find the momentum $\boldsymbol{Q}$ at which the spin susceptibility $\chi^{(s)}(\boldsymbol{Q},0)$ first diverges. $\boldsymbol{Q}$ is just the wave vector of the SDW order. The distribution pattern of the SDW moment within a unit cell is determined by the eigenvector ξ corresponding to the largest eigenvalue of $\chi^{(s)}(\boldsymbol{Q},0)$. Specifically, $\chi^{(s)}$ is a fourth-order tensor written as $\chi_{st}^{(s)pq}$. If we take combined p and q as row index and combined s and t as column index, $\chi^{(s)}$ is viewed as a 64×64 matrix. Then ξ is a normalized vector with 64 components, whose pqth component ξ_{pq} gives the relative value of the interorbital magnetic moment between the pth and qth orbital within a unit cell. For $La_3Ni_2O_7$ at AP, our RPA result suggests that ξ_{pq} is obviously nonzero only for $p=q$, which indicates on-site intraorbital magnetism. In such a situation, we define $m_p \equiv \xi_{pp}$, which gives the relative value of the magnetic moment distributed in the pth ($p=1,\ldots,8$) effective orbital within a unit cell. Note that m_p is usually a complex number whose absolute value determines the SDW amplitude while its phase angle determines the SDW phase.

When $U < U_c$, the SC would emerge. In RPA level, considering the exchange of spin fluctuations, the effective attraction can be obtained. We consider only intraband pairing between opposite momenta and perform MF treatment on the effective Hamiltonian. Hence, we can obtain the linearized gap equation near T_c, which is solved to yield the largest pairing eigenvalue λ and corresponding eigenvector $\Delta_\alpha(\boldsymbol{k})$, where α is the band index. The λ determines T_c via $T_c \propto e^{-1/\lambda}$, and the $\Delta_\alpha(\boldsymbol{k})$ determines the pairing symmetry of SC. Note that the emergence of SC is not determined by the condition $\lambda = 1$. The details of the above derivations and equations can be found in previous works [137–143].

TABLE II. The value of eight-band TB hopping parameters for $La_3Ni_2O_7$ at AP. The meaning of each superscript and subscript is the same as Table I. The unit of all parameters is eV.

	t_1^x	t_2^x	t_3^x	$t_\perp^x$	$t_\perp^{x1}$	$t_\perp^{x2}$
t	−0.403	0.045	−0.060	0.018	−0.010	0.011
t'	−0.398	0.058			−0.010	0.011
	t_1^z	t_2^z	t_3^z	$t_\perp^z$	$t_\perp^{z1}$	$t_\perp^{z2}$
t	−0.076	−0.013	−0.012	−0.597	0.013	0.009
t'	−0.104	−0.016			0.012	0.008
	t_3^{xz}	t_4^{xz}	ϵ_x	ϵ_z		
t	0.211	−0.022	0.558	0		
t'	0.190	−0.025				

[1] H. Sun, M. Huo, X. Hu, J. Li, Z. Liu, Y. Han, L. Tang, Z. Mao, P. Yang, B. Wang, J. Cheng, D.-X. Yao, G.-M. Zhang, and M. Wang, Signatures of superconductivity near 80 K in a nickelate under high pressure, Nature (London) **621**, 493 (2023).

[2] Y. Zhang, D. Su, Y. Huang, Z. Shan, H. Sun, M. Huo, K. Ye, J. Zhang, Z. Yang, Y. Xu, Y. Su, R. Li, M. Smidman, M. Wang, L. Jiao, and H. Yuan, High-temperature superconductivity with zero resistance and strange-metal behaviour in $La_3Ni_2O_{7-\delta}$, Nat. Phys. **20**, 1269 (2024).

[3] J. Hou, P.-T. Yang, Z.-Y. Liu, J.-Y. Li, P.-F. Shan, L. Ma, G. Wang, N.-N. Wang, H.-Z. Guo, J.-P. Sun, Y. Uwatoko, M. Wang, G.-M. Zhang, B.-S. Wang, and J.-G. Cheng, Emergence of high-temperature superconducting phase in pressurized $La_3Ni_2O_7$ crystals, Chin. Phys. Lett. **40**, 117302 (2023).

[4] G. Wang, N. N. Wang, X. L. Shen, J. Hou, L. Ma, L. F. Shi, Z. A. Ren, Y. D. Gu, H. M. Ma, P. T. Yang, Z. Y. Liu, H. Z. Guo, J. P. Sun, G. M. Zhang, S. Calder, J.-Q. Yan, B. S. Wang, Y. Uwatoko, and J.-G. Cheng, Pressure-induced superconductivity in polycrystalline $La_3Ni_2O_7$, Phys. Rev. X **14**, 011040 (2024).

[5] G. Wang, N. Wang, Y. Wang, L. Shi, X. Shen, J. Hou, H. Ma, P. Yang, Z. Liu, H. Zhang, X. Dong, J. Sun, B. Wang, K. Jiang, J. Hu, Y. Uwatoko, and J. Cheng, Observation of high-temperature superconductivity in the high-pressure tetragonal phase of $La_2PrNi_2O_{7-\delta}$, arXiv:2311.08212.

[6] M. Zhang, C. Pei, Q. Wang, Y. Zhao, C. Li, W. Cao, S. Zhu, J. Wu, and Y. Qi, Effects of pressure and doping on Ruddlesden-Popper phases $La_{n+1}Ni_nO_{3n+1}$, J. Mater. Sci. Technol. **185**, 147 (2024).

[7] Y. Zhou, J. Guo, S. Cai, H. Sun, P. Wang, J. Zhao, J. Han, X. Chen, Q. Wu, Y. Ding, M. Wang, T. Xiang, H. kwang Mao, and L. Sun, Investigations of key issues on the reproducibility of high-T_c superconductivity emerging from compressed $La_3Ni_2O_7$, Matter Radiat. Extremes **10**, 027801 (2025).

[8] N. Wang, G. Wang, X. Shen, J. Hou, J. Luo, X. Ma, H. Yang, L. Shi, J. Dou, J. Feng, J. Yang, Y. Shi, Z. Ren, H. Ma, P. Yang, Z. Liu, Y. Liu, H. Zhang, X. Dong, Y. Wang, K. Jiang, J. Hu, S. Calder, J. Yan, J. Sun, B. Wang, R. Zhou, Y. Uwatoko, and J. Cheng, Bulk high-temperature superconductivity in the high-pressure tetragonal phase of bilayer $La_2PrNi_2O_7$, Nature (London) **634**, 579 (2024).

[9] J. Li, P. Ma, H. Zhang, X. Huang, C. Huang, M. Huo, D. Hu, Z. Dong, C. He, J. Liao, X. Chen, T. Xie, H. Sun, and M. Wang, Identification of superconductivity in bilayer nickelate $La_3Ni_2O_7$ under high pressure up to 100 GPa, Natl. Sci. Rev., nwaf220 (2025).

[10] B. V. Beznosikov and K. S. Aleksandrov, Perovskite-like crystals of the Ruddlesden-Popper series, Cryst. Rep. **45**, 792 (2000).

[11] P. Lacorre, Passage from T-type to T′-type arrangement by reducing $R_4Ni_3O_{10}$ to $R_4Ni_3O_8$ (R = La, Pr, Nd), J. Solid State Chem. **97**, 495 (1992).

[12] Y. Zhu, D. Peng, E. Zhang, B. Pan, X. Chen, L. Chen, H. Ren, F. Liu, Y. Hao, N. Li *et al.*, Superconductivity in pressurized trilayer $La_4Ni_3O_{10-\delta}$ single crystals, Nature (London) **631**, 531 (2024).

[13] M. Zhang, C. Pei, X. Du, Y. Cao, Q. Wang, J. Wu, Y. Li, Y. Zhao, C. Li, W. Cao *et al.*, Superconductivity in trilayer nickelate $La_4Ni_3O_{10}$ under pressure, Phys. Rev. X **15**, 021005 (2025).

[14] X. Huang, H. Zhang, J. Li, M. Huo, J. Chen, Z. Qiu, P. Ma, C. Huang, H. Sun, and M. Wang, Signature of superconductivity in pressurized trilayer-nickelate $Pr_4Ni_3O_{10-\delta}$, Chin. Phys. Lett. **41**, 127403 (2024).

[15] Q. Li, Y.-J. Zhang, Z.-N. Xiang, Y. Zhang, X. Zhu, and H.-H. Wen, Signature of superconductivity in pressurized $La_4Ni_3O_{10}$, Chin. Phys. Lett. **41**, 017401 (2024).

[16] J. Yang, H. Sun, X. Hu, Y. Xie, T. Miao, H. Luo, H. Chen, B. Liang, W. Zhu, G. Qu *et al.*, Orbital-dependent electron correlation in double-layer nickelate $La_3Ni_2O_7$, Nat. Commun. **15**, 4373 (2024).

[17] L. Wang, Y. Li, S. Xie, F. Liu, H. Sun, C. Huang, Y. Gao, T. Nakagawa, B. Fu, B. Dong, Z. Cao, R. Yu, S. I. Kawaguchi, H. Kadobayashi, M. Wang, C. Jin, H. kwang Mao, and H. Liu, Structure responsible for the superconducting state in $La_3Ni_2O_7$ at low temperature and high pressure conditions, J. Am. Chem. Soc. **146**, 7506 (2024).

[18] T. Cui, S. Choi, T. Lin, C. Liu, G. Wang, N. Wang, S. Chen, H. Hong, D. Rong, Q. Wang, Q. Jin, J.-O. Wang, L. Gu, C. Ge, C. Wang, J. G. Cheng, Q. Zhang, L. Si, K. juan Jin, and E.-J. Guo, Strain mediated phase crossover in Ruddlesden Popper nickelates, Commun. Mater. **5**, 32 (2024).

[19] X. Sui, X. Han, H. Jin, X. Chen, L. Qiao, X. Shao, and B. Huang, Electronic properties of nickelate superconductor $R_3Ni_2O_7$ with oxygen vacancies, Phys. Rev. B **109**, 205156 (2024).

[20] Z. Luo, X. Hu, M. Wang, W. Wú, and D.-X. Yao, Bilayer two-orbital model of $La_3Ni_2O_7$ under pressure, Phys. Rev. Lett. **131**, 126001 (2023).

[21] Y. Zhang, L.-F. Lin, A. Moreo, and E. Dagotto, Electronic structure, dimer physics, orbital-selective behavior, and magnetic tendencies in the bilayer nickelate superconductor $La_3Ni_2O_7$ under pressure, Phys. Rev. B **108**, L180510 (2023).

[22] Y. Cao and Y.-F. Yang, Flat bands promoted by hund's rule coupling in the candidate double-layer high-temperature superconductor $La_3Ni_2O_7$ under high pressure, Phys. Rev. B **109**, L081105 (2024).

[23] Y. Zhang, L.-F. Lin, A. Moreo, T. A. Maier, and E. Dagotto, Structural phase transition, $s_{\pm}$-wave pairing, and magnetic stripe order in bilayered superconductor $La_3Ni_2O_7$ under pressure, Nat. Commun. **15**, 2470 (2024).

[24] J. Huang, Z. D. Wang, and T. Zhou, Impurity and vortex states in the bilayer high-temperature superconductor $La_3Ni_2O_7$, Phys. Rev. B **108**, 174501 (2023).

[25] B. Geisler, J. J. Hamlin, G. R. Stewart, R. G. Hennig, and P. Hirschfeld, Structural transitions, octahedral rotations, and electronic properties of $A_3Ni_2O_7$ rare-earth nickelates under high pressure, npj Quantum Mater. **9**, 38 (2024).

[26] L. C. Rhodes and P. Wahl, Structural routes to stabilize superconducting $La_3Ni_2O_7$ at ambient pressure, Phys. Rev. Mater. **8**, 044801 (2024).

[27] Y. Zhang, L.-F. Lin, A. Moreo, T. A. Maier, and E. Dagotto, Electronic structure, magnetic correlations, and superconducting pairing in the reduced Ruddlesden-Popper bilayer $La_3Ni_2O_6$ under pressure: Different role of $d_{3z^2-r^2}$ orbital compared with $La_3Ni_2O_7$, Phys. Rev. B **109**, 045151 (2024).

[28] N. Yuan, A. Elghandour, J. Arneth, K. Dey, and R. Klingeler, High-pressure crystal growth and investigation of the metal-to-metal transition of Ruddlesden–Popper trilayer nickelates $La_4Ni_3O_{10}$, J. Cryst. Growth **627**, 127511 (2024).

[29] J. Li, C.-Q. Chen, C. Huang, Y. Han, M. Huo, X. Huang, P. Ma, Z. Qiu, J. Chen, X. Hu, L. Chen, T. Xie, B. Shen, H. Sun, D. Yao, and M. Wang, Structural transition, electric transport, and electronic structures in the compressed trilayer nickelate $La_4Ni_3O_{10}$, Sci. China-Phys. Mech. Astron. **67**, 117403 (2024).

[30] B. Geisler, L. Fanfarillo, J. J. Hamlin, G. R. Stewart, R. G. Hennig, and P. Hirschfeld, Optical properties and electronic correlations in $La_3Ni_2O_{7-\delta}$ bilayer nickelates under high pressure, npj Quantum Mater. **9**, 89 (2024).

[31] H. Li, X. Zhou, T. Nummy, J. Zhang, V. Pardo, W. E. Pickett, J. F. Mitchell, and D. S. Dessau, Fermiology and electron dynamics of trilayer nickelate $La_4Ni_3O_{10}$, Nat. Commun. **8**, 704 (2017).

[32] J.-X. Wang, Z. Ouyang, R.-Q. He, and Z.-Y. Lu, Non-fermi liquid and hund correlation in $La_4Ni_3O_{10}$ under high pressure, Phys. Rev. B **109**, 165140 (2024).

[33] Y. Li, X. Du, Y. Cao, C. Pei, M. Zhang, W. Zhao, K. Zhai, R. Xu, Z. Liu, Z. Li, J. Zhao, G. Li, Y. Qi, H. Guo, Y. Chen, and L. Yang, Electronic correlation and pseudogap-like behavior of high-temperature superconductor $La_3Ni_2O_7$, Chin. Phys. Lett. **41**, 087402 (2024).

[34] M. Li, Y. Wang, C. Pei, M. Zhang, N. Li, J. Guan, M. Amboage, N.-D. Adama, Q. Kong, Y. Qi, and W. Yang, Distinguishing electronic band structure of single-layer and bilayer Ruddlesden-Popper nickelates probed by in-situ high pressure X-ray absorption near-edge spectroscopy, arXiv:2410.04230.

[35] X. Zhou, W. He, Z. Zhou, K. Ni, M. Huo, D. Hu, Y. Zhu, E. Zhang, Z. Jiang, S. Zhang, S. Su, J. Jiang, Y. Yan, Y. Wang, D. Shen, X. Liu, J. Zhao, M. Wang, M. Liu, Z. Du, and D. Feng, Revealing nanoscale structural phase separation in $La_3Ni_2O_{7-\delta}$ single crystal via scanning near-field optical microscopy, arXiv:2410.06602.

[36] G. Wang, N. Wang, T. Lu, S. Calder, J. Yan, L. Shi, J. Hou, L. Ma, L. Zhang, J. Sun, B. Wang, S. Meng, M. Liu, and J. Cheng, Chemical versus physical pressure effects on the structure transition of bilayer nickelates, npj Quantum Mater. **10**, 1 (2025).

[37] C.-Q. Chen, Z. Luo, M. Wang, W. Wú, and D.-X. Yao, Trilayer multiorbital models of $La_4Ni_3O_{10}$, Phys. Rev. B **110**, 014503 (2024).

[38] X. Chen, J. Zhang, A. S. Thind, S. Sharma, H. LaBollita, G. Peterson, H. Zheng, D. P. Phelan, A. S. Botana, R. F. Klie, and J. F. Mitchell, Polymorphism in the Ruddlesden–Popper nickelate $La_3Ni_2O_7$: Discovery of a hidden phase with distinctive layer stacking, J. Am. Chem. Soc. **146**, 3640 (2024).

[39] Z. Dong, M. Huo, J. Li, J. Li, P. Li, H. Sun, L. Gu, Y. Lu, M. Wang, Y. Wang, and Z. Chen, Visualization of oxygen vacancies and self-doped ligand holes in $La_3Ni_2O_{7-\delta}$, Nature (London) **630**, 847 (2024).

[40] F. Li, N. Guo, Q. Zheng, Y. Shen, S. Wang, Q. Cui, C. Liu, S. Wang, X. Tao, G.-M. Zhang, and J. Zhang, Design and synthesis of three-dimensional hybrid Ruddlesden-Popper nickelate single crystals, Phys. Rev. Mater. **8**, 053401 (2024).

[41] P. Puphal, P. Reiss, N. Enderlein, Y.-M. Wu, G. Khaliullin, V. Sundaramurthy, T. Priessnitz, M. Knauft, A. Suthar, L. Richter, M. Isobe, P. A. van Aken, H. Takagi, B. Keimer, Y. E. Suyolcu, B. Wehinger, P. Hansmann, and M. Hepting, Unconventional crystal structure of the high-pressure superconductor $La_3Ni_2O_7$, Phys. Rev. Lett. **133**, 146002 (2024).

[42] Q.-G. Yang, D. Wang, and Q.-H. Wang, Possible $s_{\pm}$-wave superconductivity in $La_3Ni_2O_7$, Phys. Rev. B **108**, L140505 (2023).

[43] Y.-B. Liu, J.-W. Mei, F. Ye, W.-Q. Chen, and F. Yang, $s^{\pm}$-wave pairing and the destructive role of apical-oxygen deficiencies in $La_3Ni_2O_7$ under pressure, Phys. Rev. Lett. **131**, 236002 (2023).

[44] F. Lechermann, J. Gondolf, S. Bötzel, and I. M. Eremin, Electronic correlations and superconducting instability in $La_3Ni_2O_7$ under high pressure, Phys. Rev. B **108**, L201121 (2023).

[45] H. Sakakibara, N. Kitamine, M. Ochi, and K. Kuroki, Possible high T_c superconductivity in $La_3Ni_2O_7$ under high pressure through manifestation of a nearly half-filled bilayer Hubbard model, Phys. Rev. Lett. **132**, 106002 (2024).

[46] Y. Gu, C. Le, Z. Yang, X. Wu, and J. Hu, Effective model and pairing tendency in bilayer Ni-based superconductor $La_3Ni_2O_7$, Phys. Rev. B **111**, 174506 (2025).

[47] C. Lu, Z. Pan, F. Yang, and C. Wu, Interlayer-coupling-driven high-temperature superconductivity in $La_3Ni_2O_7$ under pressure, Phys. Rev. Lett. **132**, 146002 (2024).

[48] H. Oh and Y.-H. Zhang, Type-II t-J model and shared superexchange coupling from Hund's rule in superconducting $La_3Ni_2O_7$, Phys. Rev. B **108**, 174511 (2023).

[49] Z. Liao, L. Chen, G. Duan, Y. Wang, C. Liu, R. Yu, and Q. Si, Electron correlations and superconductivity in $La_3Ni_2O_7$ under pressure tuning, Phys. Rev. B **108**, 214522 (2023).

[50] X.-Z. Qu, D.-W. Qu, J. Chen, C. Wu, F. Yang, W. Li, and G. Su, Bilayer t-J-$J_{\perp}$ model and magnetically mediated pairing in the pressurized nickelate $La_3Ni_2O_7$, Phys. Rev. Lett. **132**, 036502 (2024).

[51] Y.-F. Yang, G.-M. Zhang, and F.-C. Zhang, Interlayer valence bonds and two-component theory for high-T_c superconductivity of $La_3Ni_2O_7$ under pressure, Phys. Rev. B **108**, L201108 (2023).

[52] K. Jiang, Z. Wang, and F.-C. Zhang, High temperature superconductivity in $La_3Ni_2O_7$, Chin. Phys. Lett. **41**, 017402 (2023).

[53] Y. Zhang, L.-F. Lin, A. Moreo, T. A. Maier, and E. Dagotto, Trends in electronic structures and $s_{\pm}$-wave pairing for the rare-earth series in bilayer nickelate superconductor $R_3Ni_2O_7$, Phys. Rev. B **108**, 165141 (2023).

[54] Q. Qin and Y.-F. Yang, High-T_c superconductivity by mobilizing local spin singlets and possible route to higher T_c in pressurized $La_3Ni_2O_7$, Phys. Rev. B **108**, L140504 (2023).

[55] Y.-H. Tian, Y. Chen, J.-M. Wang, R.-Q. He, and Z.-Y. Lu, Correlation effects and concomitant two-orbital $s_{\pm}$-wave superconductivity in $La_3Ni_2O_7$ under high pressure, Phys. Rev. B **109**, 165154 (2024).

[56] R. Jiang, J. Hou, Z. Fan, Z.-J. Lang, and W. Ku, Pressure driven fractionalization of ionic spins results in cupratelike high-T_c superconductivity in $La_3Ni_2O_7$, Phys. Rev. Lett. **132**, 126503 (2024).

[57] D.-C. Lu, M. Li, Z.-Y. Zeng, W. Hou, J. Wang, F. Yang, and Y.-Z. You, Superconductivity from doping symmetric mass generation insulators: Application to $La_3Ni_2O_7$ under pressure, arXiv:2308.11195.

[58] N. Kitamine, M. Ochi, and K. Kuroki, Theoretical designing of multiband nickelate and palladate superconductors with $d^{8+\delta}$ configuration, arXiv:2308.12750.

[59] Z. Luo, B. Lv, M. Wang, W. Wú, and D.-X. Yao, High-T_c superconductivity in $La_3Ni_2O_7$ based on the bilayer two-orbital t-J model, npj Quantum Mater. **9**, 61 (2024).

[60] J.-X. Zhang, H.-K. Zhang, Y.-Z. You, and Z.-Y. Weng, Strong pairing originated from an emergent $\mathbb{Z}_2$ berry phase in $La_3Ni_2O_7$, Phys. Rev. Lett. **133**, 126501 (2024).

[61] Z. Pan, C. Lu, F. Yang, and C. Wu, Effect of rare-earth element substitution in superconducting $R_3Ni_2O_7$ under pressure, Chin. Phys. Lett. **41**, 087401 (2024).

[62] H. Sakakibara, M. Ochi, H. Nagata, Y. Ueki, H. Sakurai, R. Matsumoto, K. Terashima, K. Hirose, H. Ohta, M. Kato, Y. Takano, and K. Kuroki, Theoretical analysis on the possibility of superconductivity in the trilayer Ruddlesden-Popper nickelate $La_4Ni_3O_{10}$ under pressure and its experimental examination: Comparison with $La_3Ni_2O_7$, Phys. Rev. B **109**, 144511 (2024).

[63] H. Lange, L. Homeier, E. Demler, U. Schollwöck, A. Bohrdt, and F. Grusdt, Pairing dome from an emergent Feshbach resonance in a strongly repulsive bilayer model, Phys. Rev. B **110**, L081113 (2024).

[64] H. Yang, H. Oh, and Y.-H. Zhang, Strong pairing from doping-induced feshbach resonance and second Fermi liquid through doping a bilayer spin-one mott insulator: Application to $La_3Ni_2O_7$, Phys. Rev. B **110**, 104517 (2024).

[65] H. Lange, L. Homeier, E. Demler, U. Schollwöck, F. Grusdt, and A. Bohrdt, Feshbach resonance in a strongly repulsive bilayer model: A possible scenario for bilayer nickelate superconductors, arXiv:2309.15843.

[66] T. Kaneko, H. Sakakibara, M. Ochi, and K. Kuroki, Pair correlations in the two-orbital Hubbard ladder: Implications for superconductivity in the bilayer nickelate $La_3Ni_2O_7$, Phys. Rev. B **109**, 045154 (2024).

[67] Z. Fan, J.-F. Zhang, B. Zhan, D. Lv, X.-Y. Jiang, B. Normand, and T. Xiang, Superconductivity in nickelate and cuprate superconductors with strong bilayer coupling, Phys. Rev. B **110**, 024514 (2024).

[68] X. Wu, H. Yang, and Y.-H. Zhang, Deconfined fermi liquid to Fermi liquid transition and superconducting instability, Phys. Rev. B **110**, 125122 (2024).

[69] Y. Zhang, L.-F. Lin, A. Moreo, T. A. Maier, and E. Dagotto, Prediction of $s^{\pm}$-wave superconductivity enhanced by electronic doping in trilayer nickelates $La_4Ni_3O_{10}$ under pressure, Phys. Rev. Lett. **133**, 136001 (2024).

[70] M. Zhang, H. Sun, Y.-B. Liu, Q. Liu, W.-Q. Chen, and F. Yang, The $s^{\pm}$-wave superconductivity in the pressurized $La_4Ni_3O_{10}$, Phys. Rev. B **110**, L180501 (2024).

[71] Q.-G. Yang, K.-Y. Jiang, D. Wang, H.-Y. Lu, and Q.-H. Wang, Effective model and $s_{\pm}$-wave superconductivity in trilayer nickelate $La_4Ni_3O_{10}$, Phys. Rev. B **109**, L220506 (2024).

[72] Y. Zhang, L.-F. Lin, A. Moreo, T. A. Maier, and E. Dagotto, Electronic structure, self-doping, and superconducting instability in the alternating single-layer trilayer stacking nickelates $La_3Ni_2O_7$, Phys. Rev. B **110**, L060510 (2024).

[73] Y.-F. Yang, Decomposition of multilayer superconductivity with interlayer pairing, Phys. Rev. B **110**, 104507 (2024).

[74] S. Ryee, N. Witt, and T. O. Wehling, Quenched pair breaking by interlayer correlations as a key to superconductivity in $La_3Ni_2O_7$, Phys. Rev. Lett. **133**, 096002 (2024).

[75] C. Lu, Z. Pan, F. Yang, and C. Wu, Interplay of two E_g orbitals in superconducting $La_3Ni_2O_7$ under pressure, Phys. Rev. B **110**, 094509 (2024).

[76] Z. Ouyang, M. Gao, and Z.-Y. Lu, Absence of electron-phonon coupling superconductivity in the bilayer phase of $La_3Ni_2O_7$ under pressure, npj Quantum Mater. **9**, 80 (2024).

[77] C. Xia, H. Liu, S. Zhou, and H. Chen, Sensitive dependence of pairing symmetry on Ni-e_g crystal field splitting in the nickelate superconductor $La_3Ni_2O_7$, Nat. Commun. **16**, 1054 (2025).

[78] J. Zhan, Y. Gu, X. Wu, and J. Hu, Cooperation between electron-phonon coupling and electronic interaction in bilayer nickelates $La_3Ni_2O_7$, Phys. Rev. Lett. **134**, 136002 (2025).

[79] Y. Shen, M. Qin, and G.-M. Zhang, Effective bi-layer model hamiltonian and density-matrix renormalization group study for the high-T_c superconductivity $La_3Ni_2O_7$ under high pressure, Chin. Phys. Lett. **40**, 127401 (2023).

[80] V. Christiansson, F. Petocchi, and P. Werner, Correlated electronic structure of $La_3Ni_2O_7$ under pressure, Phys. Rev. Lett. **131**, 206501 (2023).

[81] D. A. Shilenko and I. V. Leonov, Correlated electronic structure, orbital-selective behavior, and magnetic correlations in double-layer $La_3Ni_2O_7$ under pressure, Phys. Rev. B **108**, 125105 (2023).

[82] W. Wú, Z. Luo, D.-X. Yao, and M. Wang, Superexchange and charge transfer in the nickelate superconductor $La_3Ni_2O_7$ under pressure, Sci. China-Phys. Mech. Astron. **67**, 117402 (2024).

[83] X. Chen, P. Jiang, J. Li, Z. Zhong, and Y. Lu, Critical charge and spin instabilities in superconducting $La_3Ni_2O_7$, Phys. Rev. B **111**, 014515 (2025).

[84] Z. Ouyang, J.-M. Wang, J.-X. Wang, R.-Q. He, L. Huang, and Z.-Y. Lu, Hund electronic correlation in $La_3Ni_2O_7$ under high pressure, Phys. Rev. B **109**, 115114 (2024).

[85] G. Heier, K. Park, and S. Y. Savrasov, Competing d_{xy} and $s_{\pm}$ pairing symmetries in superconducting $La_3Ni_2O_7$: LDA + FLEX calculations, Phys. Rev. B **109**, 104508 (2024).

[86] Y. Wang, K. Jiang, Z. Wang, F.-C. Zhang, and J. Hu, Electronic and magnetic structures of bilayer $La_3Ni_2O_7$ at ambient pressure, Phys. Rev. B **110**, 205122 (2024).

[87] S. Bötzel, F. Lechermann, J. Gondolf, and I. M. Eremin, Theory of magnetic excitations in multilayer nickelate superconductor $La_3Ni_2O_7$, Phys. Rev. B **109**, L180502 (2024).

[88] D. Li, K. Lee, B. Y. Wang, M. Osada, S. Crossley, H. R. Lee, Y. Cui, Y. Hikita, and H. Y. Hwang, Superconductivity in an infinite-layer nickelate, Nature (London) **572**, 624 (2019).

[89] K. Lee, B. Y. Wang, M. Osada, B. H. Goodge, T. C. Wang, Y. Lee, S. Harvey, W. J. Kim, Y. Yu, C. Murthy *et al.*, Linear-in-temperature resistivity for optimally superconducting (Nd, Sr) NiO_2, Nature (London) **619**, 288 (2023).

[90] Y. Nomura and R. Arita, Superconductivity in infinite-layer nickelates, Rep. Prog. Phys. **85**, 052501 (2022).

[91] Q. Gu and H.-H. Wen, Superconductivity in nickel-based 112 systems, The Innovation **3**, 100202 (2022).

[92] M. K. Wu, J. R. Ashburn, C. J. Torng, P. H. Hor, R. L. Meng, L. Gao, Z. J. Huang, Y. Q. Wang, and C. W. Chu, Superconductivity at 93 K in a new mixed-phase Y-Ba-Cu-O compound system at ambient pressure, Phys. Rev. Lett. **58**, 908 (1987).

[93] P. A. Lee, N. Nagaosa, and X.-G. Wen, Doping a mott insulator: Physics of high-temperature superconductivity, Rev. Mod. Phys. **78**, 17 (2006).

[94] A. Schilling, M. Cantoni, J. D. Guo, and H. R. Ott, Superconductivity above 130 K in the Hg-Ba-Ca-Cu-O system, Nature (London) **363**, 56 (1993).

[95] Y. Kamihara, T. Watanabe, M. Hirano, and H. Hosono, Iron-based layered superconductor $La[O_{1-x}F_x]FeAs(x = 0.05 \sim 0.12)$ with $T_c = 26$ K, J. Am. Chem. Soc. **130**, 3296 (2008).

[96] R. Zhi-An, L. Wei, Y. Jie, Y. Wei, S. Xiao-Li, Zheng-Cai, C. Guang-Can, D. Xiao-Li, S. Li-Ling, Z. Fang, and Z. Zhong-Xian, Superconductivity at 55 K in iron-based f-doped layered quaternary compound $Sm[O_{1-x}F_x]$ FeAs, Chin. Phys. Lett. **25**, 2215 (2008).

[97] E. K. Ko, Y. Yu, Y. Liu, L. Bhatt, J. Li, V. Thampy, C.-T. Kuo, B. Y. Wang, Y. Lee, K. Lee, J.-S. Lee, B. H. Goodge, D. A. Muller, and H. Y. Hwang, Signatures of ambient pressure superconductivity in thin film $La_3Ni_2O_7$, Nature (London) **638**, 935 (2025).

[98] G. Zhou, W. Lv, H. Wang, Z. Nie, Y. Chen, Y. Li, H. Huang, W. Chen, Y. Sun, Q.-K. Xue, and Z. Chen, Ambient-pressure superconductivity onset above 40 K in $(La,Pr)_3Ni_2O_7$, Nature **640**, 641 (2025).

[99] T. Fukamachi, Y. Kobayashi, T. Miyashita, and M. Sato, ^{139}La NMR studies of layered perovskite systems $La_3Ni_2O_{7-\delta}$ and $La_4Ni_3O_{10}$, J. Phys. Chem. Solids **62**, 195 (2001).

[100] R. Khasanov, T. J. Hicken, D. J. Gawryluk, L. P. Sorel, S. Bötzel, F. Lechermann, I. M. Eremin, H. Luetkens, and Z. Guguchia, Pressure-induced split of the density wave transitions in $La_3Ni_2O_{7-\delta}$, Nat. Phys. **21**, 430 (2025).

[101] K. Chen, X. Liu, J. Jiao, M. Zou, C. Jiang, X. Li, Y. Luo, Q. Wu, N. Zhang, Y. Guo *et al.*, Evidence of spin density waves in $La_3Ni_2O_{7-\delta}$, Phys. Rev. Lett. **132**, 256503 (2024).

[102] Z. Dan, Y. Zhou, M. Huo, Y. Wang, L. Nie, M. Wang, T. Wu, and X. Chen, Spin-density-wave transition in double-layer nickelate $La_3Ni_2O_7$, Sci. Bull. **70**, 1239 (2025).

[103] X. Chen, J. Choi, Z. Jiang, J. Mei, K. Jiang, J. Li, S. Agrestini, M. Garcia-Fernandez, X. Huang, H. Sun, D. Shen, M. Wang, J. Hu, Y. Lu, K.-J. Zhou, and D. Feng, Electronic and magnetic excitations in $La_3Ni_2O_7$, Nat. Commun. **15**, 9597 (2024).

[104] Z. Liu, H. Sun, M. Huo, X. Ma, Y. Ji, E. Yi, L. Li, H. Liu, J. Yu, Z. Zhang, Z. Chen, F. Liang, H. Dong, H. Guo, D. Zhong, B. Shen, S. Li, and M. Wang, Evidence for charge and spin density waves in single crystals of $La_3Ni_2O_7$ and $La_3Ni_2O_6$, Sci. China-Phys. Mech. Astron. **66**, 217411 (2023).

[105] M. Kakoi, T. Oi, Y. Ohshita, M. Yashima, K. Kuroki, T. Kato, H. Takahashi, S. Ishiwata, Y. Adachi, N. Hatada, T. Uda, and H. Mukuda, Multiband metallic ground state in multilayered nickelates $La_3Ni_2O_7$ and $La_4Ni_3O_{10}$ probed by ^{139}La-NMR at ambient pressure, J. Phys. Soc. Jpn. **93**, 053702 (2024).

[106] T. Xie, M. Huo, X. Ni, F. Shen, X. Huang, H. Sun, H. C. Walker, D. Adroja, D. Yu, B. Shen, L. He, K. Cao, and M. Wang, Strong interlayer magnetic exchange coupling in $La_3Ni_2O_{7-\delta}$ revealed by inelastic neutron scattering, Sci. Bull. **69**, 3221 (2024).

[107] N. K. Gupta, R. Gong, Y. Wu, M. Kang, C. T. Parzyck, B. Z. Gregory, N. Costa, R. Sutarto, S. Sarker, A. Singer, D. G. Schlom, K. M. Shen, and D. G. Hawthorn, Anisotropic spin stripe domains in bilayer $La_3Ni_2O_7$, arXiv:2409.03210.

[108] J.-J. Feng, T. Han, J.-P. Song, M.-S. Long, X.-Y. Hou, C.-J. Zhang, Q.-G. Mu, and L. Shan, Unaltered density wave transition and pressure-induced signature of superconductivity in Nd-doped $La_3Ni_2O_7$, Phys. Rev. B **110**, L100507 (2024).

[109] Y. Meng, Y. Yang, H. Sun, S. Zhang, J. Luo, M. Wang, F. Hong, X. Wang, and X. Yu, Density-wave-like gap evolution in $La_3Ni_2O_7$ under high pressure revealed by ultrafast optical spectroscopy, Nat. Commun. **15**, 10408 (2024).

[110] S. Fan, Z. Luo, M. Huo, Z. Wang, H. Li, H. Yang, M. Wang, D.-X. Yao, and H.-H. Wen, Tunneling spectra with gaplike features observed in nickelate $La_3Ni_2O_7$ at ambient pressure, Phys. Rev. B **110**, 134520 (2024).

[111] M. Xu, G. C. Jose, A. Rutherford, H. Wang, S. Zhang, R. J. Cava, H. Zhou, W. Bi, and W. Xie, Pressure-induced phase transitions in bilayer $La_3Ni_2O_7$, arXiv:2410.18840.

[112] Y. Li, Y. Cao, L. Liu, P. Peng, H. Lin, C. Pei, M. Zhang, H. Wu, X. Du, W. Zhao, K. Zhai, X. Zhang, J. Zhao, M. Lin, P. Tan, Y. Qi, G. Li, H. Guo, L. Yang, and L. Yang, Distinct ultrafast dynamics of bilayer and trilayer nickelate superconductors regarding the density-wave-like transitions, Sci. Bull. **70**, 180 (2025).

[113] G. Wu, J. J. Neumeier, and M. F. Hundley, Magnetic susceptibility, heat capacity, and pressure dependence of the electrical resistivity of $La_3Ni_2O_7$ and $La_4Ni_3O_{10}$, Phys. Rev. B **63**, 245120 (2001).

[114] Z. Liu, M. Huo, J. Li, Q. Li, Y. Liu, Y. Dai, X. Zhou, J. Hao, Y. Lu, M. Wang, and H.-H. Wen, Electronic correlations and partial gap in the bilayer nickelate $La_3Ni_2O_7$, Nat. Commun. **15**, 7570 (2024).

[115] J. Zhang, D. Phelan, A. Botana, Y.-S. Chen, H. Zheng, M. Krogstad, S. G. Wang, Y. Qiu, J. Rodriguez-Rivera, R. Osborn *et al.*, Intertwined density waves in a metallic nickelate, Nat. Commun. **11**, 6003 (2020).

[116] S. Xu, C.-Q. Chen, M. Huo, D. Hu, H. Wang, Q. Wu, R. Li, D. Wu, M. Wang, D.-X. Yao *et al.*, Origin of the density wave instability in trilayer nickelate $La_4Ni_3O_{10}$ revealed by optical and ultrafast spectroscopy, Phys. Rev. B **111**, 075140 (2025).

[117] X. Du, Y. Li, Y. Cao, C. Pei, M. Zhang, W. Zhao, K. Zhai, R. Xu, Z. Liu, Z. Li *et al.*, Correlated electronic structure and density-wave gap in trilayer nickelate $La_4Ni_3O_{10}$, arXiv:2405.19853.

[118] B. Zhang, C. Xu, and H. Xiang, Emergent spin-charge-orbital order in superconductor $La_3Ni_2O_7$, arXiv:2407.18473.

[119] I. V. Leonov, Electronic correlations and spin-charge-density stripes in double-layer $La_3Ni_2O_7$, arXiv:2410.15298.

[120] H. LaBollita, V. Pardo, M. R. Norman, and A. S. Botana, Assessing the formation of spin and charge stripes in $La_3Ni_2O_7$ from first-principles, Phys. Rev. Mater. **8**, L111801 (2024).

[121] X.-S. Ni, Y. Ji, L. He, T. Xie, D.-X. Yao, M. Wang, and K. Cao, Spin density wave in the bilayered nickelate $La_2Ni_2O_{7-\delta}$ at ambient pressure, npj Quantum Mater. **10**, 17 (2025).

[122] X.-W. Yi, Y. Meng, J.-W. Li, Z.-W. Liao, W. Li, J.-Y. You, B. Gu, and G. Su, Nature of charge density waves and metal-insulator transition in pressurized $La_3Ni_2O_7$, Phys. Rev. B **110**, L140508 (2024).

[123] K.-Y. Jiang, Y.-H. Cao, Q.-G. Yang, H.-Y. Lu, and Q.-H. Wang, Theory of pressure dependence of superconductivity in bilayer nickelate $La_3Ni_2O_7$, Phys. Rev. Lett. **134**, 076001 (2025).

[124] Y. Chen, Y.-H. Tian, J.-M. Wang, R.-Q. He, and Z.-Y. Lu, Non-Fermi liquid and antiferromagnetic correlations with hole doping in the bilayer two-orbital Hubbard model of $La_3Ni_2O_7$ at zero temperature, Phys. Rev. B **110**, 235119 (2024).

[125] Y. Zhang, L.-F. Lin, A. Moreo, T. A. Maier, and E. Dagotto, Magnetic correlations and pairing tendencies of the hybrid stacking nickelate superlattice $La_7Ni_5O_{17}$ ($La_3Ni_2O_7$/$La_4Ni_3O_{10}$) under pressure, arXiv:2408.07690.

[126] L.-F. Lin, Y. Zhang, N. Kaushal, G. Alvarez, T. A. Maier, A. Moreo, and E. Dagotto, Magnetic phase diagram of a two-orbital model for bilayer nickelates varying doping, Phys. Rev. B **110**, 195135 (2024).

[127] C. Qin, K. Foyevtsova, L. Si, G. A. Sawatzky, and M. Jiang, Intertwined charge and spin density wave state of $La_3Ni_2O_7$, arXiv:2410.15649.

[128] I. V. Leonov, Electronic structure and magnetic correlations in the trilayer nickelate superconductor $La_4Ni_3O_{10}$ under pressure, Phys. Rev. B **109**, 235123 (2024).

[129] H. LaBollita, V. Pardo, M. R. Norman, and A. S. Botana, Electronic structure and magnetic properties of $La_3Ni_2O_7$ under pressure: Active role of the Ni-$d_{x^2-y^2}$ orbitals, arXiv:2309.17279.

[130] Y. Mochizuki, H. Akamatsu, Y. Kumagai, and F. Oba, Strain-engineered peierls instability in layered perovskite $La_3Ni_2O_7$ from first principles, Phys. Rev. Mater. **2**, 125001 (2018).

[131] V. Voronin, I. Berger, V. Cherepanov, L. Gavrilova, A. Petrov, A. Ancharov, B. Tolochko, and S. Nikitenko, Neutron diffraction, synchrotron radiation and exafs spectroscopy study of crystal structure peculiarities of the lanthanum nickelates $La_{n+1}Ni_nO_y$ (n =1,2,3), Methods Phys. Res. A **470**, 202 (2001).

[132] G. Kresse and J. Furthmüller, Efficient iterative schemes for ab initio total-energy calculations using a plane-wave basis set, Phys. Rev. B **54**, 11169 (1996).

[133] J. P. Perdew, A. Ruzsinszky, G. I. Csonka, O. A. Vydrov, G. E. Scuseria, L. A. Constantin, X. Zhou, and K. Burke, Restoring the density-gradient expansion for exchange in solids and surfaces, Phys. Rev. Lett. **100**, 136406 (2008).

[134] G. Kresse and D. Joubert, From ultrasoft pseudopotentials to the projector augmented-wave method, Phys. Rev. B **59**, 1758 (1999).

[135] A. I. Liechtenstein, V. I. Anisimov, and J. Zaanen, Density-functional theory and strong interactions: Orbital ordering in Mott-Hubbard insulators, Phys. Rev. B **52**, R5467(R) (1995).

[136] A. A. Mostofi, J. R. Yates, Y.-S. Lee, I. Souza, D. Vanderbilt, and N. Marzari, WANNIER90: A tool for obtaining maximally-localised Wannier functions, Comput. Phys. Commun. **178**, 685 (2008).

[137] T. Takimoto, T. Hotta, and K. Ueda, Strong-coupling theory of superconductivity in a degenerate Hubbard model, Phys. Rev. B **69**, 104504 (2004).

[138] K. Yada and H. Kontani, Origin of weak pseudogap behaviors in $Na_{0.35}CoO_2$: Absence of small hole pockets, J. Phys. Soc. Jpn. **74**, 2161 (2005).

[139] K. Kubo, Pairing symmetry in a two-orbital Hubbard model on a square lattice, Phys. Rev. B **75**, 224509 (2007).

[140] S. Graser, T. Maier, P. Hirschfeld, and D. Scalapino, Near-degeneracy of several pairing channels in multiorbital models for the Fe pnictides, New J. Phys. **11**, 025016 (2009).

[141] F. Liu, C.-C. Liu, K. Wu, F. Yang, and Y. Yao, $d + id'$ chiral superconductivity in bilayer silicene, Phys. Rev. Lett. **111**, 066804 (2013).

[142] M. Zhang, J.-J. Hao, X. Wu, and F. Yang, Lifshitz transition enhanced triplet p_z-wave superconductivity in hydrogen-doped KCr_3As_3, Phys. Rev. B **105**, 134509 (2022).

[143] K. Kuroki, S. Onari, R. Arita, H. Usui, Y. Tanaka, H. Kontani, and H. Aoki, Unconventional pairing originating from the disconnected Fermi surfaces of superconducting $LaFeAsO_{1-x}F_x$, Phys. Rev. Lett. **101**, 087004 (2008).

[144] B. Y. Wang, Y. Zhong, S. Abadi, Y. Liu, Y. Yu, X. Zhang, Y.-M. Wu, R. Wang, J. Li, Y. Tarn, E. K. Ko, V. Thampy, M. Hashimoto, D. Lu, Y. S. Lee, T. P. Devereaux, C. Jia, H. Y. Hwang, and Z.-X. Shen, Electronic structure of compressively strained thin film $La_2PrNi_2O_7$, arXiv:2504.16372.